Atmos. Chem. Phys., 6, 4705–4722, 2006
www.atmos-chem-phys.net/6/4705/2006/

Atmospheric Chemistry and Physics

Ground-based remote sensing of HDO/H_2O ratio profiles: introduction and validation of an innovative retrieval approach

M. Schneider, F. Hase, and T. Blumenstock

IMK-ASF, Forschungszentrum Karlsruhe and Universität Karlsruhe, Germany

Received: 3 May 2006 – Published in Atmos. Chem. Phys. Discuss.: 27 June 2006
Revised: 5 October 2006 – Accepted: 19 October 2006 – Published: 20 October 2006

Abstract. We propose an innovative approach for analysing ground-based FTIR spectra which allows us to detect variabilities of lower and middle/upper tropospheric HDO/H_2O ratios. We show that the proposed method is superior to common approaches. We estimate that lower tropospheric HDO/H_2O ratios can be detected with a noise to signal ratio of 15% and middle/upper tropospheric ratios with a noise to signal ratio of 50%. The method requires the inversion to be performed on a logarithmic scale and to introduce an inter-species constraint. While common methods calculate the isotope ratio posterior to an independent, optimal estimation of the HDO and H_2O profile, the proposed approach is an optimal estimator for the ratio itself. We apply the innovative approach to spectra measured continuously during 15 months and present, for the first time, an annual cycle of tropospheric HDO/H_2O ratio profiles as detected by ground-based measurements. Outliers in the detected middle/upper tropospheric ratios are interpreted by backward trajectories.

1 Introduction

Water vapour is the dominant greenhouse gas in the Earth's atmosphere. However, its concentration, evolution, and transport processes are still poorly understood. This is in particularly true for the upper half of the troposphere and the lower stratosphere, a region crucial for the Earth's radiation balance. Climate models would widely benefit from further measurements of water vapour at these altitudes and from an improved knowledge of its vertical transport processes. However, the quick changes of atmospheric water vapour concentrations with time, their large horizontal gradients, and their decrease of several orders of magnitude with height make their accurate detection a challenging task for any measurement technique. Schneider et al. (2006) showed that ground-based FTIR spectroscopy, performed from mountain observatories, allows for the detection of H_2O variabilities up to the tropopause. Compared to other techniques measuring H_2O like ptu-sondes or Lidars, the FTIR measurements also allow the retrieval of HDO amounts. Variations in the HDO/H_2O ratio act as markers for the source and history of the water vapour and thus may provide valuable information about its transport processes and the dynamical situation of the troposphere. In Gedzelman (1988) it is shown that low middle tropospheric HDO/H_2O ratios are correlated to high atmospheric stability, typical for anticyclonic conditions, and that high HDO/H_2O ratios are prevailing under statically unstable conditions. The HDO/H_2O ratio is commonly given in form of a δD value, which is the relative difference of the actual HDO/H_2O ratio to a standard HDO/H_2O ratio (here we apply SMOW (Standard Mean Ocean Water): R_S=3.1152×10^{-4}) in per mil:

$$\delta\mathrm{D} = 1000 \times \left(\frac{[\mathrm{HDO}]/[\mathrm{H_2O}]}{R_S} - 1 \right) \quad (1)$$

So far there exist no continuous measurements of δD throughout the whole troposphere. Up to date such measurements have only been performed in form of a few campaigns (Taylor, 1972; Ehhalt, 1974; Zahn, 2001). New satellite sensors may allow continuous measurements, which are only limited by the life time of the satellite. Kuang et al. (2003) applies ATMOS data to determine HDO/H_2O ratio throughout the tropical tropopause. Other space-borne experiments like MIPAS, ACE, or ODIN also have the potential of detecting this ratio down to the tropopause. For altitudes from the tropopause to the surface and over longer time scales ground-based FTIR measurements have a unique potential of continuously monitoring δD values. In this paper we show that common retrieval methods are not able to provide useful information about the vertical δD distribution. We demonstrate that for this purpose the innovative approach presented here

Correspondence to: M. Schneider
(matthias.schneider@imk.fzk.de)

Published by Copernicus GmbH on behalf of the European Geosciences Union.

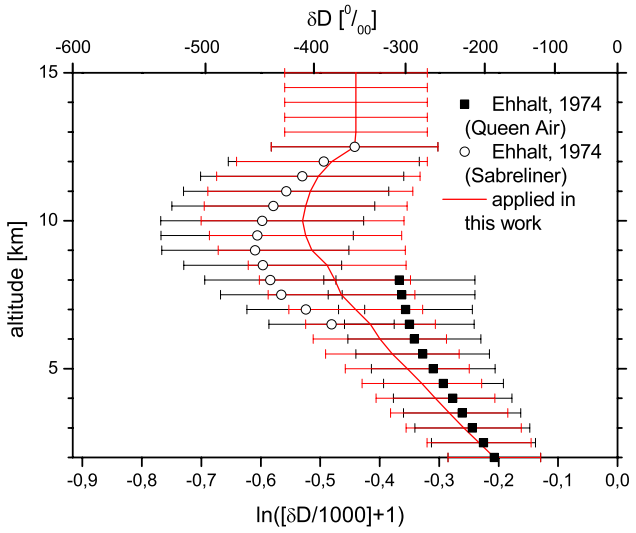

Fig. 1. Typical δD profile and its variability as derived from the data of Ehhalt (1974). Black crosses: Queen Air flights; black circles: Sabreliner flights; red line: a-priori δD applied in this work.

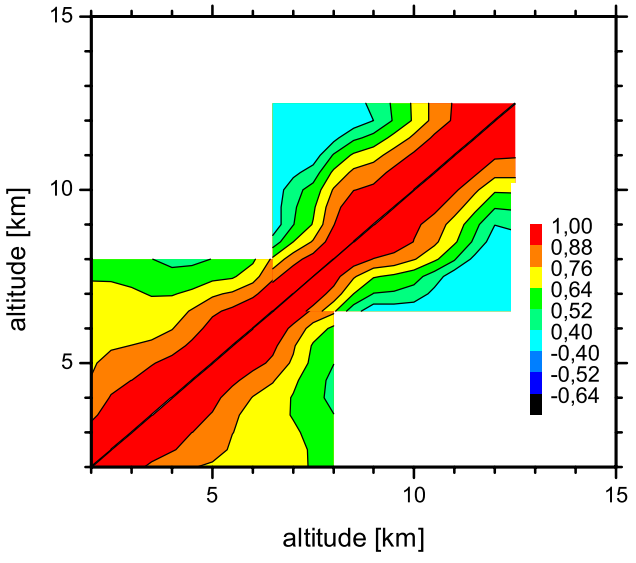

Fig. 2. δD a-priori correlation matrix as derived from the data of Ehhalt (1974).

has to be applied. In addition this approach supports the development of innovative satellite retrieval codes.

2 A-priori knowledge of HDO and H_2O

Tropospheric water vapour mixing ratios are log-normally distributed. This was shown, for example, in Schneider et al. (2006) by an analysis of ptu-sonde data measured from 1999 to 2003. Measurements of HDO/H_2O profiles are relatively rare. One of the most extensive HDO/H_2O datasets is from Ehhalt (1974). It consists of measurements performed during two major phases. During the first phase, between 1965 and 1967, the Queen Air 80 airplane was used as platform. It allowed to measure up to an altitude of 9 km. The second phase in 1971/72 focused on higher altitudes. The applied Sabreliner airplane allowed to reach altitudes up to 13 km. Figure 1 collects these measurements. It shows the mean δD and its variability (as error bars). The mean Sabreliner values systematically exceed the mean Queen Air values. The reason might be the locations of the measurements: while the Queen Air data are from a variety of measurement sites (continental mid-latitudes, marine subtropical region,...), the Sabreliner data are mainly from a continental mid-latitude site (Scottsbluff, Nebraska). In this work we assumed a δD profile for Izaña as depicted as red line in Fig. 1. Above 13 km we assumed a δD value of -350, which is in good agreement with Abbas et al. (1987).

Besides the mean and the variability, the Ehhalt (1974) data may give information about the typical correlations of the HDO/H_2O ratio between different altitudes. Figure 2 shows the relevant correlation matrix ($\mathbf{\Gamma}_a$). The covariance matrix is calculated from $\mathbf{\Gamma}_a$ by $\mathbf{S}_a = \mathbf{\Sigma}_a \mathbf{\Gamma}_a \mathbf{\Sigma}_a^T$, where $\mathbf{\Sigma}_a$ is a diagonal matrix containing the variabilities for a certain altitude. It is found that both datasets yield similar correlation patterns in the overlapping altitude region. For the lower troposphere the correlation length (distance within the correlation coefficient reduces to $e^{-1/2}$) is 5 km and with increasing altitudes it rapidly decreases. Above 5 km it is around 2.5 km. For the simulations performed in this work we constructed a HDO profile for each H_2O profile, in the way that the ensemble as a whole obeys the HDO/H_2O statistics derived from the Ehhalt (1974) data. This is possible by assuming that $\frac{\delta D}{1000}+1$ is log-normally distributed. This is a justified assumption since the δD values are to a large extent concentrated close to a Rayleigh distillation curve but turbulent and convective transport occasionally produce very high δD values: δD is more log-normal than normal distributed. On logarithmic scale Eq. (1) can be rewritten as:

$$\ln([\mathrm{HDO}]) = \ln(\frac{\delta \mathrm{D}}{1000} + 1) + \ln(R_S) + \ln([\mathrm{H_2O}]) \qquad (2)$$

From the Ehhalt (1974) data we derive the mean and covariance of $\ln(\frac{\delta D}{1000}+1)$, which we apply to simulate HDO profiles for the whole ensemble of H_2O profiles. The ensemble of H_2O profiles is the same as in Schneider et al. (2006). The profile pairs are used for the theoretical error estimation and sensitivity assessment shown in Sect. 5.

3 General retrieval aspects

In this study PROFFIT (Hase et al., 2004) is the inversion code used. It applies the Karlsruhe Optimised and Precise Radiative Transfer Algorithm (KOPRA, Höpfner et al., 1998; Kuntz et al., 1998; Stiller et al., 1998) as the forward model,

which was developed for the analysis of MIPAS-Envisat limb sounder spectra. PROFFIT enables the inversion on a linear and logarithmic scale. The code does not employ a fixed a-priori value for the measurement noise. This value is taken from the residuals of the fit itself, performing an automatic adjustment of the constraints. Furthermore, if the observed absorptions depend on temperature, PROFFIT allows the retrieval of temperature profiles.

We analysed H_2O and HDO signatures in the mid-infrared (between 700–1400 cm^{-1}). For H_2O we applied the signatures of Schneider et al. (2006). Due to the low abundances of HDO in comparison to H_2O its absorption structures are weaker. Furthermore the strongest HDO lines are generally superimposed by strong H_2O absorptions. The spectroscopic atlas of Meier et al. (2004) was applied in the search for suited HDO lines. We found the 3 lines shown in Fig. 3 to be a good choice. They are relatively strong and they are detectable even on days with large atmospheric water vapour content. However, they have strong interferences from N_2O and CH_4. In particular for the latter the spectroscopic description is not satisfactory, which is responsible for the main part of the residuals. The spectral windows shown in Fig. 3 are for an atmosphere with moderately saturated H_2O absorption lines and with a lower tropospheric slant column (2.3–4.3 km) amount of $2.2\times10^{22}cm^{-2}$. In Sects. 5 and 6 we show that under this condition it is still possible to retrieve middle/upper tropospheric δD values. Besides N_2O and CH_4, O_3 is an important absorber in the analysed microwindows. All the sharp lines seen in the H_2O microwindows are due to this trace gas. Further interfering absorbers are $H_2^{18}O$, CO_2, HNO_3, and COF_2. For this reason and in addition to the H_2O and HDO profiles, we simultaneously retrieve profiles of $H_2^{18}O$, CO_2, N_2O and CH_4, O_3, HNO_3, and COF_2, whereby for the latter two this is done by simply scaling their climatological profiles. The state vector consists of mixing ratios of all absorbers and the temperature at 41 atmospheric levels and the spectral shift and ordinate scale in each microwindow. The applied temperature data are a combination of the data from the local ptu-sondes (up to 30 km) and data supplied by the automailer system of the Goddard Space Flight Center. To account for uncertainties in the temperature data we also retrieve simultaneously the temperature profiles.

The spectroscopic line parameters of H_2O and its isotopes, and of O_3 are taken from the HITRAN 2004 database (Rothman et al., 2005) for all other species they are from HITRAN 2000 (Rothman et al., 2003).

4 Introduction of the innovative retrieval approach

Ground-based FTIR spectroscopy, if performed from mountain observatories, allows the detection of water vapour variabilities up to the tropopause (Schneider et al., 2006). The atmospheric HDO absorptions are weaker than the H_2O absorption, but it should also be possible to retrieve HDO variabilities at least up to the middle/upper troposphere. Aiming on HDO/H_2O ratio profiles, a common retrieval approach consists in retrieving maximum a-posteriori profiles for both H_2O and HDO, and the subsequent calculation of their ratios. However, this leads generally not to the most probable HDO/H_2O ratio profiles. The reason is that this common method disregards an important probability density function (pdf) when formulating the Bayesian a-posteriori pdf: the pdf of the HDO/H_2O ratio profiles. In this case the H_2O and HDO profiles are retrieved completely independently from each other, and the ratio between them is a ratio of two independently remote-sensed profiles with different vertical resolutions and sensitivities. The comparison of such remote-sensed profiles is, however, not straight forward (Rodgers and Connor, 2003). If the objective is to obtain a maximum a-posteriori solution of the HDO/H_2O ratio profile (or of the δD profile), the pdf of the δD profiles must be taken into account. The relatively small variances of this pdf are responsible for the very strong correlations between both species: a typical variability of δD of 70 means that knowing the H_2O mixing ratio, the HDO mixing ratio only has a remaining uncertainty of 7%. This is much less than the typical HDO and H_2O variabilities of around 100%. The pdf of the δD profiles must be considered when formulating the Bayesian a-posteriori pdf. On a logarithmic scale the δD statistics converts into a statistics of the difference between the logarithms of H_2O and HDO profiles (see Eq. 2). Thus, it can be characterised, in analogy to the individual H_2O and HDO statistics, in form of a covariance matrix. The cost function, which

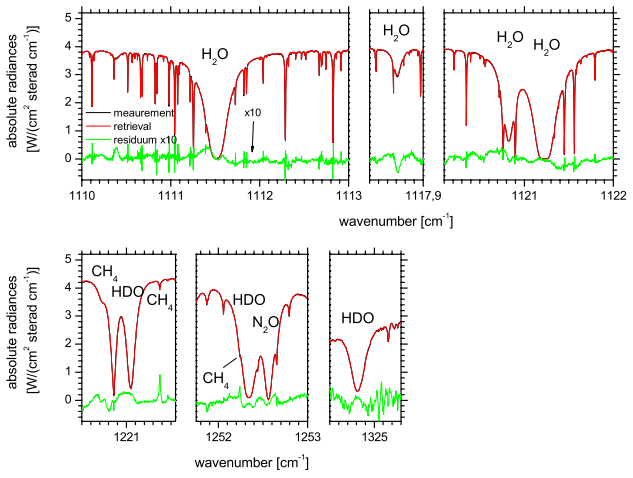

Fig. 3. Spectral windows applied. Plotted is the situation for a real measurement taken on 24 January 2005 (solar elevation angle 20.5°; lower tropospheric slant column (2.3–4.3 km) of 2.2×10^{22} cm^{-2}). Upper panel: H_2O windows; lower panel: HDO windows; black line: measured spectrum; red line: simulated spectrum; green line: difference between simulation and measurement multiplied by 10.

is proportional to the negative logarithm of the Bayesian a-posteriori pdf, can then be written as:

$$\sigma^{-2}(\boldsymbol{y}-\mathbf{K}\boldsymbol{x})^T(\boldsymbol{y}-\mathbf{K}\boldsymbol{x})+(\boldsymbol{x}-\boldsymbol{x}_a)^T\mathbf{B}^T\mathbf{B}(\boldsymbol{x}-\boldsymbol{x}_a) +(\boldsymbol{x}-\boldsymbol{x}_a)^T(\mathbf{C}^T\mathbf{C}+\mathbf{D}^T\mathbf{D})(\boldsymbol{x}-\boldsymbol{x}_a) \quad (3)$$

Here the first two terms form the commonly applied cost function, i.e. when the δD statistics is disregarded. $\mathbf{K}$ and σ are the Jacobian and the measurement noise, $\boldsymbol{y}$, $\boldsymbol{x}$, and $\boldsymbol{x}_a$ represent the spectrum, the state vector, and the a-priori state vector. $\mathbf{B}^T\mathbf{B}$ accounts for the pdfs of the ln[H_2O] and ln[HDO] profiles. $\mathbf{B}^T\mathbf{B}$ has only entries for elements which link a species with itself (individual constraints), i.e. for matrix areas around the diagonal. Matrix areas connecting different species have all elements with value 0. In the case of a 3 level atmosphere it has the form:

$$\mathbf{B}^T\mathbf{B}=\begin{pmatrix}\mathbf{S}^{-1}_{a,H_2O} & \begin{matrix}0&0&0\\0&0&0\\0&0&0\end{matrix}\\ \begin{matrix}0&0&0\\0&0&0\\0&0&0\end{matrix} & \mathbf{S}^{-1}_{a,\mathrm{HDO}}\end{pmatrix}$$

whereby $\mathbf{S}_{a,\mathrm{H_2O}}$ and $\mathbf{S}_{a,\mathrm{HDO}}$ are the a-priori covariances for ln[H_2O] and ln[HDO].

The last term of Eq. (3) takes care of the most important aspects of the δD statistics. One important aspect is the statistics of the difference of the ln[H_2O] and ln[HDO] mixing ratios, without the consideration of interlevel correlations of these differences. Considering the corresponding pdf when formulating the Bayesian a-posteriori pdf provides for a diagonal constraint of the δD state vector. The matrix $\mathbf{C}$ is of the form:

$$\mathbf{C}=\begin{pmatrix}\frac{1}{\sqrt{c_1}}&0&0&-\frac{1}{\sqrt{c_1}}&0&0\\0&\frac{1}{\sqrt{c_2}}&0&0&-\frac{1}{\sqrt{c_2}}&0\\0&0&\frac{1}{\sqrt{c_3}}&0&0&-\frac{1}{\sqrt{c_3}}\\0&0&0&0&0&0\\0&0&0&0&0&0\\0&0&0&0&0&0\end{pmatrix}$$

and thus:

$$\mathbf{C}^T\mathbf{C}=\begin{pmatrix}\frac{1}{c_1}&0&0&-\frac{1}{c_1}&0&0\\0&\frac{1}{c_2}&0&0&-\frac{1}{c_2}&0\\0&0&\frac{1}{c_3}&0&0&-\frac{1}{c_3}\\-\frac{1}{c_1}&0&0&\frac{1}{c_1}&0&0\\0&-\frac{1}{c_2}&0&0&\frac{1}{c_2}&0\\0&0&-\frac{1}{c_3}&0&0&\frac{1}{c_3}\end{pmatrix}$$

whereby c_n is the variance of ln[HDO]$-$ ln[H_2O] at layer n. In contrast to $\mathbf{B}^T\mathbf{B}$, $\mathbf{C}^T\mathbf{C}$ has large entries in the matrix area linking ln[H_2O] with ln[HDO] mixing ratios.

A second important aspect of the δD statistics is the difference between the slopes of ln[H_2O] and ln[HDO]. Slope means here the difference in ln[H_2O] or ln[HDO] between neighbouring layers. Introducing the pdf of this measure into the Bayesian a-posteriori pdf constrains the slope of the δD profiles. The matrix $\mathbf{D}$ is of the form:

$$\mathbf{D}=\begin{pmatrix}\frac{1}{\sqrt{d_1}}&-\frac{1}{\sqrt{d_1}}&0&-\frac{1}{\sqrt{d_1}}&\frac{1}{\sqrt{d_1}}&0\\0&\frac{1}{\sqrt{d_2}}&-\frac{1}{\sqrt{d_2}}&0&-\frac{1}{\sqrt{d_2}}&\frac{1}{\sqrt{d_2}}\\0&0&0&0&0&0\\0&0&0&0&0&0\\0&0&0&0&0&0\\0&0&0&0&0&0\end{pmatrix}$$

and thus:

$$\mathbf{D}^T\mathbf{D} = \begin{pmatrix} \frac{1}{d_1} & -\frac{1}{d_1} & 0 & -\frac{1}{d_1} & \frac{1}{d_1} & 0 \\ -\frac{1}{d_1} & (\frac{1}{d_1}+\frac{1}{d_2}) & -\frac{1}{d_2} & \frac{1}{d_1} & -(\frac{1}{d_1}+\frac{1}{d_2}) & \frac{1}{d_2} \\ 0 & -\frac{1}{d_2} & \frac{1}{d_2} & 0 & \frac{1}{d_2} & -\frac{1}{d_2} \\ -\frac{1}{d_1} & \frac{1}{d_1} & 0 & \frac{1}{d_1} & -\frac{1}{d_1} & 0 \\ \frac{1}{d_1} & -(\frac{1}{d_1}+\frac{1}{d_2}) & \frac{1}{d_2} & -\frac{1}{d_1} & (\frac{1}{d_1}+\frac{1}{d_2}) & -\frac{1}{d_2} \\ 0 & \frac{1}{d_2} & -\frac{1}{d_2} & 0 & -\frac{1}{d_2} & \frac{1}{d_2} \end{pmatrix}$$

whereby d_n is the variance of the slope difference of ln[HDO] and ln[H_2O] at layer n.

The latest PROFFIT version (version 9.4) has the option to add inter-species constraints to the cost function. Performing the retrieval on a logarithmic scale and applying $\mathbf{C}^T\mathbf{C}+\mathbf{D}^T\mathbf{D}$ as described above in Eq. (3), considers the most important contributions of the δD pdf to the Bayesian a-posteriori pdf. Thus, our proposed method provides for a statistically optimal solution of the δD profiles. Currently PROFFIT is the only code applied for the retrieval of trace gas profiles from FTIR spectra, which has these options. It is thus the only code allowing for an optimal estimation of ratio profiles from ground-based FTIR spectra.

5 Theoretical validation of retrieval approaches

The detection of middle/upper tropospheric δD variabilities by ground-based measurements is even more challenging than the detection of H_2O or HDO variabilities. The small variabilities in δD require a very high precision of the retrieved δD values. The variability of δD is more than one order of magnitude smaller than the variability of HDO: for a known H_2O amount, the remaining variability of HDO is only 7% compared to the absolute HDO variability of 100%. However, HDO and H_2O respond similarly to the error sources, so the HDO/H_2O ratios are automatically more precise than individually retrieved HDO or H_2O amounts. In this section we examine if the common approach already leads to a sufficient precision or whether it is necessary to apply our proposed approach. A formalism for an analytic error estimation of remote sensed data is suggested by Rodgers (2000). It requires linearity of the problem. However, the retrieval of water vapour, especially if performed on a logarithmic scale, involves important nonlinearities. Therefore, in this study we perform the error estimations in full treatment (Monte Carlo method) by means of the ensemble of the H_2O and corresponding HDO profiles, as described in Sect. 2. We make forward calculations for each single pair of H_2O and HDO profiles. Subsequently we perform two retrievals for each error estimation: a first with correct parameters and a second with erroneous parameters. The parameter error is then given by the difference of the two retrievals. The smoothing error is the difference between the retrieval with correct parameter and the original profile (the profile assumed for the forward calculation).

Table 1. Assumed uncertainties.

error source	uncertainty
measurement noise	S/N of 500
phase error	0.01 rad
modulation eff.	1%
T profile[a]	up to 2.5 K at surface 1 K rest of troposphere
solar elevation angle	0.1°
line intensity	+5%
pres. broad. coef. (pc_A)	+1%
pres. broad. coef. (pc_B)	±1%

[a] detailed description see text

As parameter errors we consider measurement noise, uncertainties in solar elevation angle, instrumental line shape (ILS: parameterised as modulation efficiency and phase error; Hase et al., 1999), temperature profile, and spectroscopic parameters (line intensity and pressure broadening coefficient). The assumed parameter uncertainties are listed in Table 1. All these error sources are considered when estimating the total error. In Schneider et al. (2006) it is shown that for water vapour the smoothing error and errors due to measurement noise, uncertainties in the phase error, uncertainties in the temperature profile, and uncertainties in the pressure broadening coefficient are important. Thus, their associated retrieval errors are analysed in more detail. Two sources are considered as errors in the temperature profile: firstly, the measurement uncertainty of the sonde, which is assumed to be 0.5 K throughout the whole troposphere and to have no interlevel correlations. Secondly, the temporal differences between the FTIR and the sonde's temperature measurements, which are estimated to be 1.5 K at the surface and 0.5 K in the rest of the troposphere, with 5 km correlation length for the interlevel correlations. We also consider two aspects of uncertainties in the spectroscopic pressure broadening coefficients: pc_A accounts for correlated uncertainties of the HDO and H_2O pressure broadening coefficient. We assumed that both the HDO and H_2O HITRAN coefficients overestimate the real value by 1%. The error pc_B considers inconsistencies between the HDO and H_2O coefficients. We assumed 1% too small H_2O and 1% too large HDO coefficients.

Errors are commonly presented as a mean error ($\overline{\hat{x}-x}$), which represents the systematic error component, and an error variance ($\sigma_\epsilon^2 = \sum_{i=1}^{n}(\hat{x}_i-x_i)^2/(n-1)$), which represents

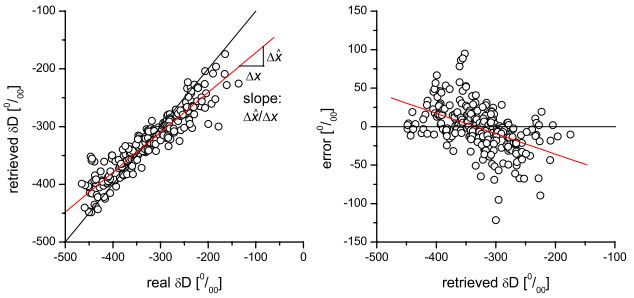

Fig. 4. Characteristic of smoothing error for 5.3–8.8 km represented as correlation of original δD and δD retrieved with correct parameters and for no measurement noise. Left panel: black line: diagonal; black crosses: ensemble members; red line: linear least squares fit to ensemble members; right panel: dependence of error on retrieved amount (sensitivity error).

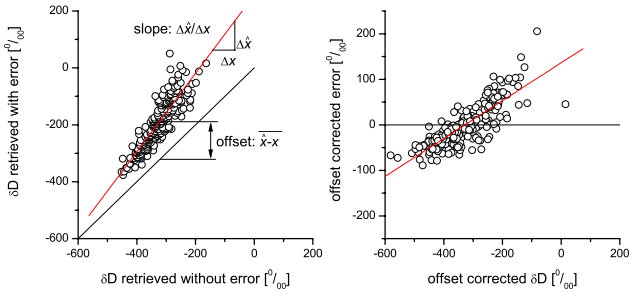

Fig. 5. Same as Fig. 4, but for error due to inconsistency in pressure broadening coefficients of HDO and H_2O.

the random error component. Here x is the correct amount, $\hat{x}$ the erroneously retrieved amount, and n the number of measurements. This method occasionally overestimates the random error. A good example is the smoothing error. If the a-priori assumptions are correct it has no mean error. Nevertheless, it has a systematic component: the sensitivity. Generally at higher altitudes the δD retrieval is less sensitive to real atmospheric variabilities than at low altitudes. At high altitudes the δD values below the a-priori value are overestimated and the δD values above the a-priori value are underestimated. Figure 4 shows an example. It depicts the situation for the smoothing error as obtained from our simulations for the retrieval with inter-species constraint and for the middle troposphere (5.3–8.8 km). The left panel depicts the correlation between the original and the retrieved δD (simulation of smoothing error, i.e. no application of parameter errors and no measurement noise). Separating the errors only in a mean and covariance disregards the fact that for low δD the error is mainly positive and for high δD mainly negative (see right panel). This systematic error behavior is then contributed to the random error. For the error estimation in this work, we not only consider the mean error, but also the dependency of the error on δD, as systematic component. Therefore, we perform the error estimation by means of least squares fits. This approach was already applied in Schneider et al. (2006) to demonstrate the systematic error behavior of a linear and logarithmic retrieval of water vapour amounts. It enables a better separation of systematic error components from random components. The regression curves of the least squares fits demonstrate how the real atmosphere – as a mean – is mapped by the retrieval: their difference from the diagonal describes the systematic error component. Its offset to the diagonal at the a-priori value is the mean error, i.e. $\overline{\hat{x}-x}$, and the difference of its slope from unity gives the dependency of the error from the δD value. In the following we call it the sensitivity error. Figure 5, shows the same as Fig. 4, but for the error due to inconsistencies in the spectroscopic data of HDO and H_2O. This error source produces for the 5.3–8.8 km layer both a mean error of +40%, indicated as offset in the left panel, and a sensitivity error of +40%. Here and in the following the mean error percentile is the ratio of the mean error and the mean retrieved δD value, and the percentile of the sensitivity error is the difference of the regression line slope from unity. Disregarding the overestimation of sensitivity, as in the example of Fig. 5, would overestimate the random error component.

In this method of error estimation the random errors are given by the scattering around the regression curve, the error variance $\sigma^2_{\epsilon_{\rm reg}} = \sum_{i=0}^{n} (\hat{x}_i - \hat{x}_{{\rm reg},i})^2/(n-1)$. The $\hat{x}_{\rm reg}$ values are the $\hat{x}$ values as predicted by the regression curve. Applying least squares fits, the scattering around the regression curve can easily be calculated from the correlation coefficient ρ: the overall variance of the retrieved amounts ($\sigma^2_{\hat{x}} = \sum_{i=0}^{n} (\hat{x}_i - \overline{\hat{x}_i})^2/(n-1)$) is the sum of the variance of the population of the regression curve ($\sigma^2_{\rm reg} = \sum_{i=0}^{n} (\hat{x}_{{\rm reg},i} - \overline{\hat{x}_i})^2/(n-1)$) and the error variance:

$$\sigma^2_{\hat{x}} = \sigma^2_{\rm reg} + \sigma^2_{\epsilon_{\rm reg}} \quad (4)$$

Since ρ^2 is the ratio between the variance of the population of the regression curve and the overall variance ($\rho^2 = \sigma^2_{\rm reg}/\sigma^2_{\hat{x}}$) we can express the random error relative to the overall variability (noise to signal error) in form of:

$$\frac{\sigma_{\epsilon_{\rm reg}}}{\sigma_{\hat{x}}} = \sqrt{1-\rho^2} \quad (5)$$

In statistical textbooks (e.g., Wilks, 1995) the aforementioned relations are generally derived for the sum of squares and not for the variances. Here we applied variances (sum of squares divided by $(n-1)$) to put emphasis on the analogy to the common error treatment. In the following the random error is always presented as $\sigma_{\epsilon_{\rm reg}}/\sigma_{\hat{x}}$.

The sensitivity of a retrieval is commonly characterised by its averaging kernels. In the case of a strong absorber like water vapour the kernels strongly depend on the actual

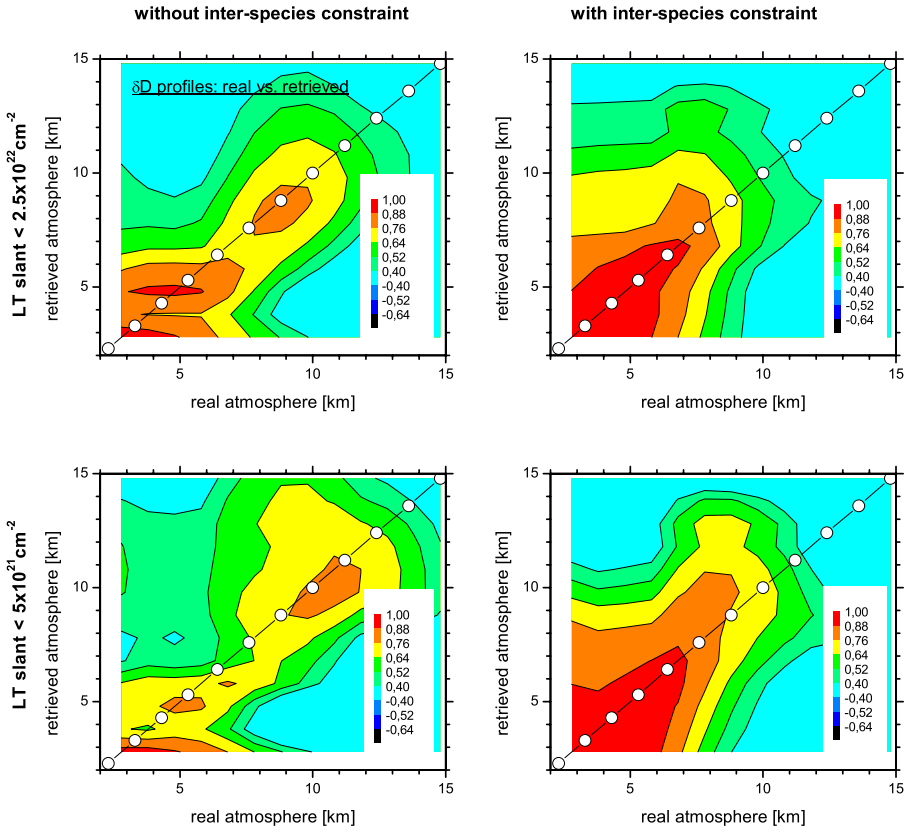

Fig. 6. Estimated correlation matrices between the real and retrieved δD values for 1 km partial columns in the absence of parameter errors. Left panels: without inter-species constraints; right panels: with inter-species constraint; upper panels: for LT slant $<2.5\times10^{22}$cm^{-2}; lower panels: for LT slant $<5\times10^{21}$cm^{-2}. Colors mark the values of the correlation coefficients (ρ) as given in legend.

atmospheric water vapour content and there is no typical averaging kernel. Furthermore, variability of water vapor is 10 000 ppmv at the surface and 3–5 ppmv at the tropopause, i.e. it varies over nearly four orders of magnitude. This fact is not taken into account in the standard description of averaging kernels and thus their interpretation is not straight forward. Applying kernels on logarithmic scale would be an improvement, however, they still depend on the actual atmospheric state, i.e. they are largely variable. Therefore, instead of averaging kernels we present the retrieval sensitivity in form of correlation matrices obtained from our error simulation. They show the correlation between a large ensemble of real atmospheric profiles and the corresponding retrieved profiles. They give a realistic overview of what atmospheric regions are detectable with the retrieval. Furthermore, introducing parameter errors in the simulations allows us to perform this sensitivity analysis for a realistic error scenario, whereas the averaging kernels only present the situation in the absence of parameter errors. However, parameter errors have a large influence on the retrieval's sensitivity (compare Fig. 6 to Fig. 17) and should thus be considered when presenting the vertical resolution.

We found that for lower tropospheric slant columns (2.3–4.3 km; subsequently called LT slant) above 2.5×10^{22}cm^{-2} the degrees of freedom of the HDO profile begin to decrease sharply. Under these conditions the HDO absorption are widely masked by H_2O band absorptions. Furthermore, then the H_2O lines are clearly saturated, which limits the H_2O sensitivity to the lower and middle troposphere. As a consequence, reasonable δD profiles are only detectable when the condition LT slant $<2.5\times10^{22}$cm^{-2} is fulfilled. In the following we will only examine measurements performed under this condition (more than 90% of all Izaña measurements). We would like to remark, that reasonable δD values for the total columns can be calculated for much larger lower tropospheric water vapour amounts.

In addition, we examine the errors and sensitivities for unsaturated H_2O lines, which is fulfilled for LT slant $<5\times10^{21}$cm^{-2}. Under this condition the sensitivities with respect to middle/upper tropospheric H_2O and HDO should be further increased. Since these conditions are generally given at the Jungfraujoch and Mauna Loa FTIR sites, it is a good estimation of the quality of δD profiles achievable at these sites. At Izaña this condition is only fulfilled for 10% of all measurements.

Table 2. Estimated noise/signal error of δD for our innovative approach of the total column, the lower troposphere (2.3–5.3 km) and the middle/upper troposphere [%] for LT slant $<2.5\times10^{22}$cm^{-2}. Respective errors of the common approach are given in parenthesis.

error source	total	2.3–5.3 km	5.3–8.8 km	6.4–10.0 km
smoothing	2(2)	4(8)	31(66)	56(69)
meas. noise	2(3)	3(23)	17(74)	18(67)
pha. err.	0(0)	0(1)	0(1)	0(1)
T. profile	0(0)	0(8)	1(22)	2(9)
pres. coef. pc_A	0(1)	2(9)	13(17)	23(16)
pres. coef. pc_B	2(2)	14(51)	44(92)	71(95)
total	3(4)	15(57)	50(99)	82(94)

Table 3. Same as Table 2 but for LT slant $<5\times10^{21}$cm^{-2}.

error source	total	2.3–5.3 km	5.3–8.8 km	6.4–10.0 km
smoothing	2(2)	7(11)	32(76)	52(76)
meas. noise	2(3)	5(28)	11(79)	12(75)
pha. err.	0(0)	0(1)	1(4)	1(4)
T. profile	0(0)	0(14)	1(22)	1(14)
pres. coef. pc_A	0(0)	1(5)	3(12)	5(11)
pres. coef. pc_B	1(1)	17(47)	29(73)	34(63)
total	3(4)	18(48)	40(94)	61(100)

5.1 Smoothing error

The smoothing error is generally the most important error for profiles retrieved from ground-based FTIR spectra. It is due to the limited information content of the spectra, which prevents the detection of fine structures in the vertical distribution of the retrieved species. Figure 6 shows correlation matrices between the profiles retrieved from the simulated spectra and the original profiles. At this stage we introduced no parameter errors and no measurement noise. It shows the sensitivity of the retrievals if only the smoothing error was present. In order to get the same averaging kernels as for the retrieval of spectra with measurement noise, we multiplied the first terms of the cost function (3) with a fixed σ^{-2} corresponding to a signal to noise ratio of 500. Figure 6 demonstrates that our approach, compared to the common approach, better resolves 1 km fine structures, at least for altitudes below 8 km. The common approach may be suited to map the situation close to the surface (ρ of 0.92 at 3 km) but it tracks poorly the real atmospheric variabilities around 7 km, even for the LT slant $<5\times10^{21}$cm^{-2} condition (ρ of 0.55). Around 9 km it performs better (ρ of 0.72). To the contrast, our approach leads to a very good correlation at all altitudes up to 8–9 km, for the LT slant $<2.5\times10^{22}$cm^{-2} as well as the LT slant $<5\times10^{21}$cm^{-2} condition. For the latter the retrieved and real amounts at 7 and 9 km still correlate with a coefficient of 0.89 and 0.73, respectively.

Figure 7 shows the random smoothing error as calculated from Eq. (5). It is the proportion of the variability seen in the retrieved data that is not due to real atmospheric variabilities. The lines represent the smoothing error when considering structures as fine as 1 km. Black lines are for the LT slant $<2.5\times10^{22}$cm^{-2} condition and red lines for the LT slant $<5\times10^{21}$cm^{-2} condition. It summarises the observations made by Fig. 6: the smoothing error of the common retrieval limits the detection of small scale structures to the lowest atmospheric layers, whereas our innovative approach allows for their detection up to 8–9 km. At 7 km and for the LT slant $<5\times10^{21}$cm^{-2} 46% of the retrieved variabilities are caused by the smoothing error but still 54% are due to real variabilities (see red line in right panel). At the same altitude the common method yields to an error of 84%.

The structures retrievable by the common approach are very rough. As a consequence this approach prohibits a satisfactory separation of the variabilities above 4 km from those occurring within the boundary layer, even for very thick layers. This can be seen in the left panel of Fig. 7. The symbols show the error for rougher structures (layers between 3 and 3.6 km as indicated by the error bars). Black circles represent the situation for LT slant $<2.5\times10^{22}$cm^{-2} and red crosses for LT slant $<5\times10^{21}$cm^{-2}. While the lower troposphere (2.3–5.3 km) may be detectable with a satisfactory precision (8%), at higher altitudes the errors get very large (e.g. 66% for layer between 5.3–8.8 km). On the contrary, the structures retrievable by our approach are fine enough to separate middle/upper tropospheric variabilities from lower tropospheric variabilities. This results in a very precise detection of the lower tropospheric variability (6%) and satisfactory precision for the middle/upper troposphere (e.g. 31% for the 5.3–8.8 km layer). This is collected in Tables 2 and 3, which shows the random errors calculated for a lower (2.3–5.3 km), middle (5.3–8.8 km), and upper tropospheric layer (6.4–10.0 km), and for the total column for the common and our approach. The values of the common approach are presented in brackets.

Figure 8 shows the systematic smoothing error as derived from the offset and slope of the least squares fits. It is the aforementioned mean and sensitivity error. Both approaches have similar systematic errors. The retrievals are less sensible for higher altitudes than for low altitudes. This is due to the weaker spectroscopic signatures from the former as compared to the latter.

5.2 Measurement noise error

Figures 9 and 10 show the errors due to measurement noise. This error source is different for each absorption line. The produced error is, thus, not common to HDO and H_2O. Consequently, it is very large in case of the common approach, in particular when fine structures are considered. Then the error is situated above 50% even close to the surface. In the free troposphere it reaches 90%. Introducing inter-species

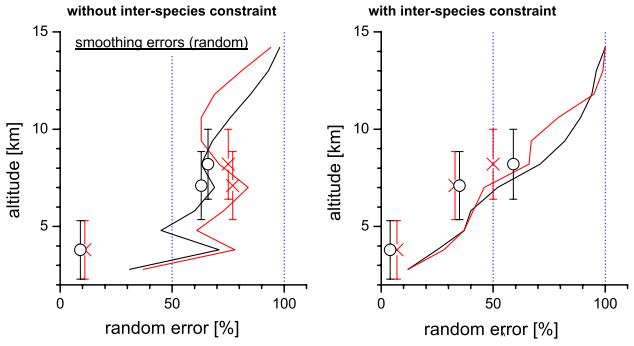

Fig. 7. Estimated random smoothing errors. Lines are for 1 km broad layers. Symbols indicate smoothing errors for thicker layers (2.3–5.3, 5.3–8.8, and 6.4–10.0 km as indicated by error bars). Black: for LT slant $<2.5\times10^{22}$cm^{-2}; red: for LT slant $<5\times10^{21}$cm^{-2}; left panel: without inter-species constraint; right panel: with inter-species constraint.

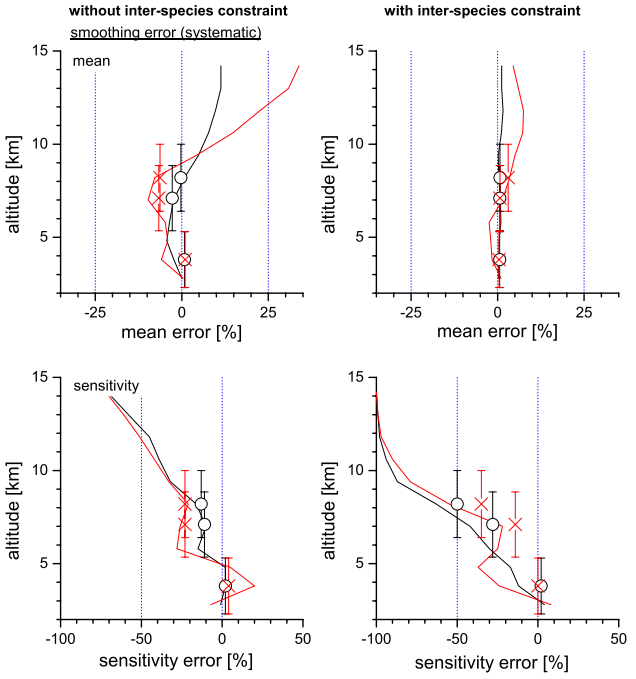

Fig. 8. Estimated systematic smoothing errors. Upper panels show the mean error, lower panel the sensitivity error. The meaning of lines and symbols is the same as in Fig. 7.

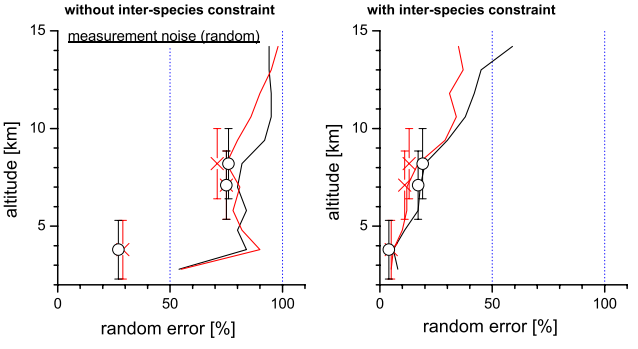

Fig. 9. Same as in Fig. 7 but for errors due to measurement noise.

constraints widely reduces the error. It prevents the H_2O and HDO profiles from responding independently to the error. Their responses must be in accordance to the δD statistics. By this means a similar response of H_2O and HDO to the measurement noise is forced, although it is a not common error source. The error becomes as small as 5% at the surface and 10% at 7 km.

Figure 10 shows the systematic error due to measurement noise. It is interesting to observe that the measurement noise, a pure random error source, produces quite large systematic errors for the common approach. The reason is, that the retrieved δD are not statistically optimal solutions. Our approach provides for a statistically optimal solution and the measurement noise only produces random errors.

5.3 Temperature error

Figure 11 shows the random errors due to uncertainties in the temperature profile. The error source is common to all lines, but due to different temperature sensitivities the error responses differ. Consequently, in case of the common retrieval the error is large. Even for thick layers it ranges from 8% (lower troposphere) to above 20% for the middle/upper troposphere. With the inter-species constraints the HDO and H_2O profiles respond similar to an error in the temperature profile. As the right panel demonstrates the respective impact on the δD profile is much smaller as compared to the common retrieval. Then the temperature error has very small impact on the retrieval (1% in the middle/upper troposphere).

The temperature error is a pure random error source. Similar to the measurement noise the retrieval with inter-species constraints produces no systematic error. On contrary, the common approach provides for no statistically optimal solution and it produces systematic errors, which are, however, below 5% at all altitudes.

5.4 ILS error

In Fig. 12 we present our error estimation for the phase error uncertainties of the instrument. Its interpretation is similar to the interpretation of the temperature error. The common approach yields somehow larger errors since H_2O and HDO respond individually and in a different manner to the error source. On the other hand our approach assures a very similar response and thus eliminates the error. Systematic errors can be neglected (below 1% for all altitudes).

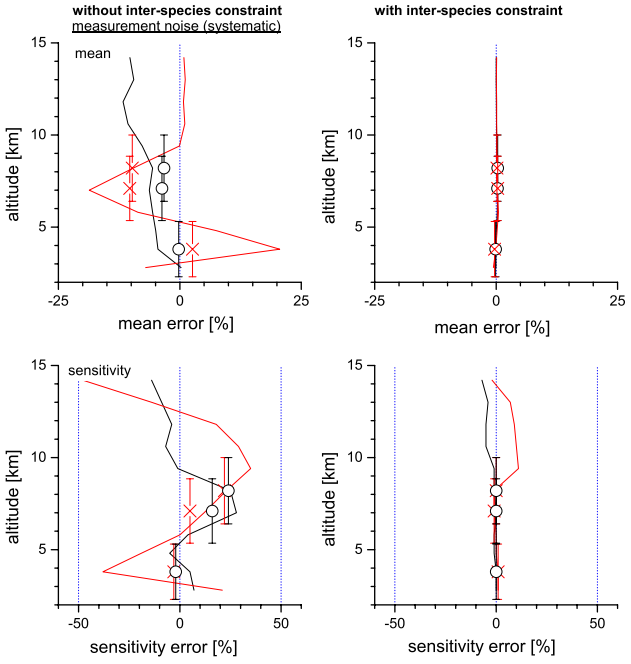

Fig. 10. Same as Fig. 8 but for errors due to measurement noise.

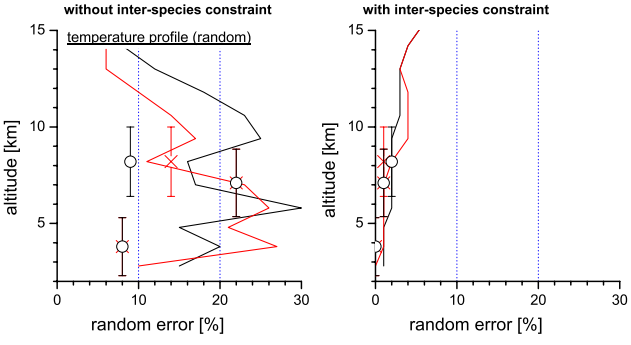

Fig. 11. Same as in Fig. 7 but for errors due to uncertainties of the temperature profile.

5.5 Pressure broadening coefficient error

We consider two kinds of errors concerning the pressure broadening coefficient (γ). Firstly, we assume that the errors of both the γ of H_2O and HDO are completely correlated, and secondly, that there is an inconsistency in the γ of H_2O and HDO, i.e. the errors of γ of both isotopologues are not correlated with each other. For example, the error for γ of HDO is by 2% larger than the error for γ of H_2O.

Although, both error sources are systematic, they produce large random errors. This is due to non-linearities, which cause an interaction of the parameter errors with the smoothing error. The impact of an erroneous parameter depends on the actual averaging kernel. And vice versa: an erroneous γ produces important alteration in the spectra. It worsens the fit quality and thus affects the averaging kernels.

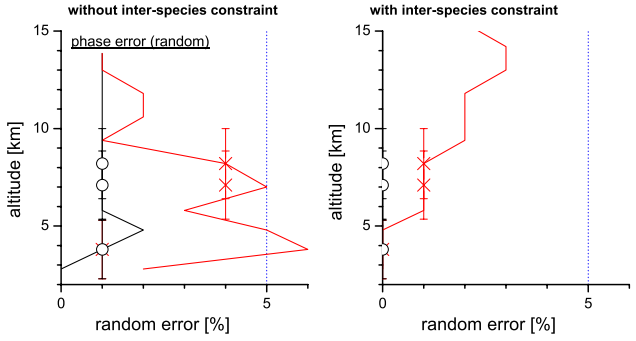

Fig. 12. Same as Fig. 7 but for errors due to uncertainties in the phase error.

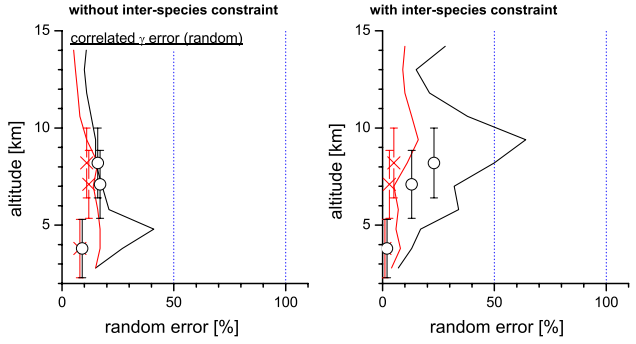

Fig. 13. Same as Fig. 7 but for errors due to correlated errors in the pressure broadening coefficients.

5.5.1 Correlated errors of H_2O and HDO pressure broadening coefficients

This error source is common to both HDO and H_2O lines. However, the lines have different intensities and temperature dependence. Consequently the error response of HDO and H_2O differs. Figure 13 presents the random error component if both the γ of H_2O and HDO are overestimated by 1%. Considering fine structures (red and black lines) there is not much difference between both retrieval methods. The common retrieval even performs slightly better in the upper troposphere. The impact of this error is larger than the impact of the ILS or temperature error. In this case the inter-species constraint is not able to force a similar response of the H_2O and HDO profile. For that purpose we would need to artificially strengthen the inter-species constraint. If we consider rough structures our approach produces smaller random errors than the common approach, at least for altitudes below 6 km. In Tables 2 and 3 these errors are collected as pc_A errors.

The systematic error components are shown in Fig. 14. Increasing the pressure broadening coefficient systematically changes the altitude dependence of the retrieval's sensitivity. The common method produces large mean and sensitivity

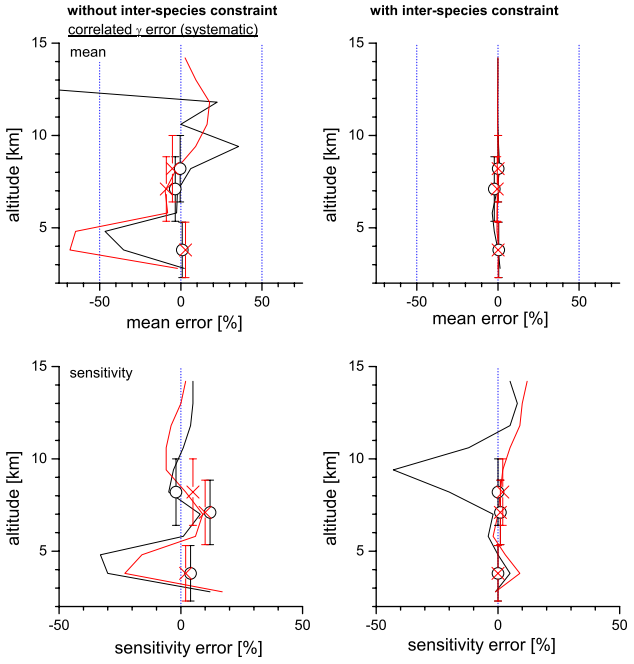

Fig. 14. Same as Fig. 8 but for errors due to correlated errors in the pressure broadening coefficients.

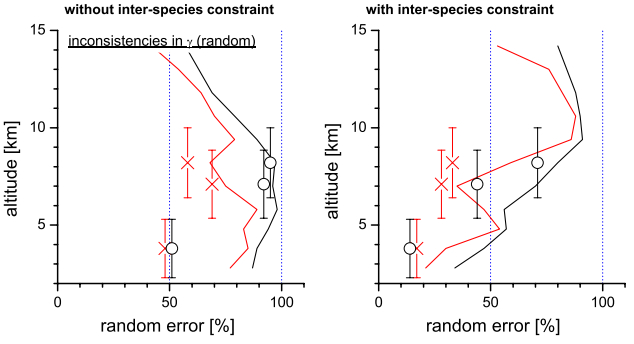

Fig. 15. Same as Fig. 7 but for errors due to inconsistencies in the pressure broadening coefficients.

errors at nearly all altitudes, in particular if fine structures are considered. Introducing the inter-species constraints reduces the systematic error. It nearly eliminates the mean error and has very low sensitivity errors below 8 km, even considering fine structures. However, at higher altitudes the inter-species constraint is weaker (due to higher a-priori δD variability). We find that around 10 km the sensitivity error is somehow accumulated.

5.5.2 Inconsistency in errors of H_2O and HDO pressure broadening coefficient

This error source is different for HDO and H_2O. Consequently, it should produce large errors. This can be observed in Figs. 15 and 16. We assume that the broadening coefficient of HDO is erroneously 2% too large as compared to the H_2O coefficient. This produces large random and systematic errors. This inconsistencies are together with the smoothing error the most important error source. They are collected in Tables 2 and 3 as pc_B errors. However, we should keep in mind the limitations in separating the parameter errors from the smoothing errors. As a consequence the presented error is not independent from the smoothing error. Nevertheless, we can conclude that, our approach reduces this error as compared to the common approach. This is true for the random as well as the systematic error component.

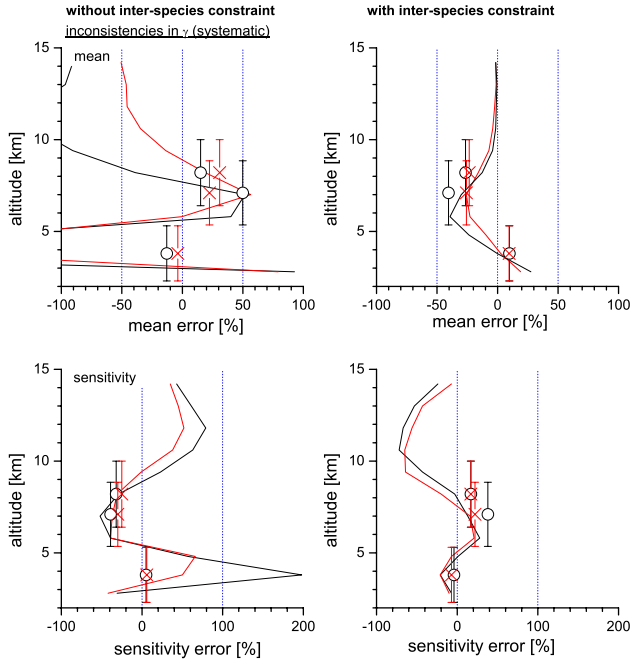

Fig. 16. Same as Fig. 8 but for errors due to inconsistencies in the pressure broadening coefficients.

5.6 Total error

The total error cannot be simply calculated as the root mean square of the parameter errors and the smoothing errors. Due to interactions between them the errors are not independent. For this reason we have to make an extra simulation of the total error. Figures 17 and 18 are the same as Figs. 6 and 7 but taking into account the realistic parameter errors as listed in Table 1. The additional errors reduce the coefficients of correlation between the retrieved and the real δD. The detailed error estimation indicates that this is mainly caused by the uncertainties in the pressure broadening coefficients and the measurement noise. However, our approach still enables to get fine structures at 7 km (ρ of 0.81 if LT slant $<5\times10^{21}$cm^{-2}). This situation is summarised in Fig. 18. Furthermore, it shows that, for a realistic error scenario, our approach enables the retrieval of middle tropospheric δD

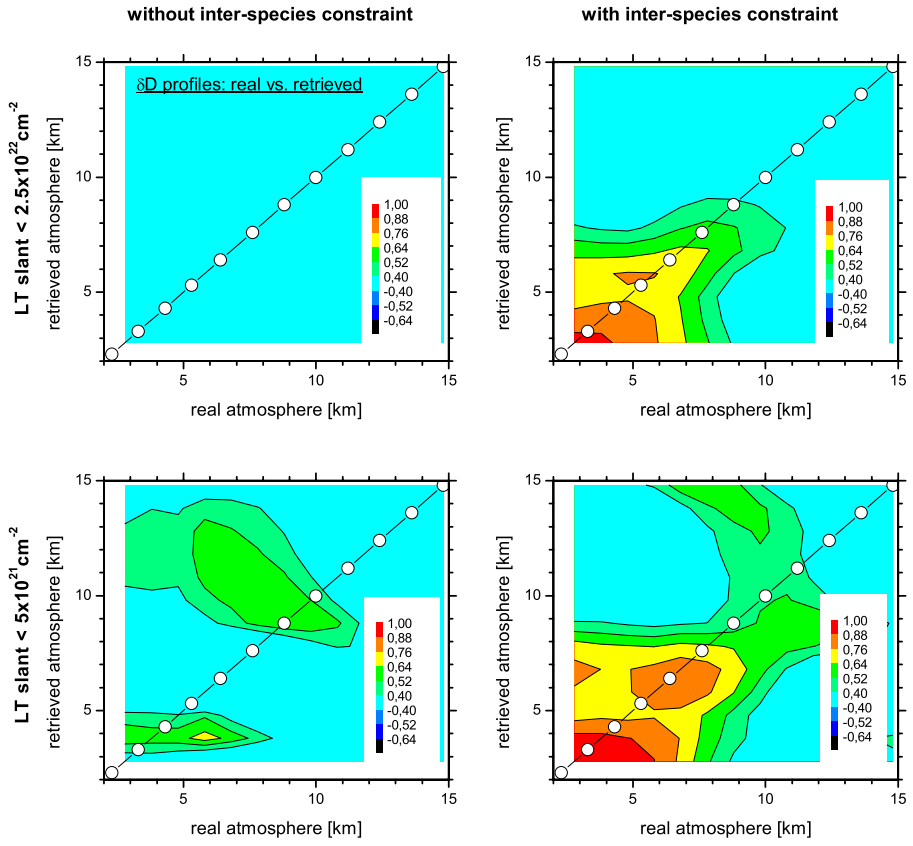

Fig. 17. Same as Fig. 6 but for consideration of all error sources.

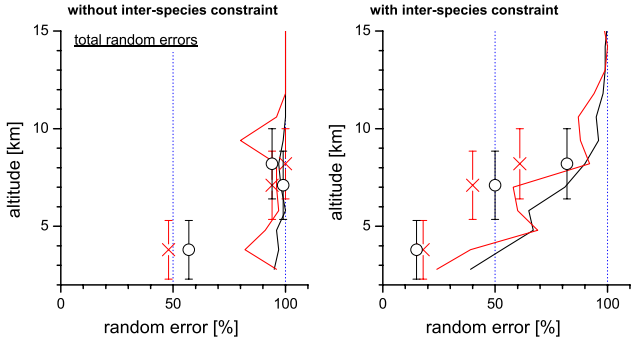

Fig. 18. Same as Fig. 7 but for consideration of all error sources.

values even for moderately saturated H_2O lines with a noise to signal error of 50%. That means, that 50% of all the variability seen in the retrieved amount is due to real atmospheric variabilities. The common approach only allows the retrieval of lower tropospheric δD values with a precision of 57%, compared to the 15% of our method at this altitude, and it is useless for the retrieval of middle tropospheric δD values. When the LT slant $<5\times10^{21}\,\mathrm{cm}^{-2}$ criterion is fulfilled, i.e. for nearly all measurements performed at Mauna Loa or Jungfraujoch, our approach even allows the detection of upper tropospheric δD values with an estimated precision of 61%.

Tables 2 and 3 collect the estimated random errors. Our approach not only enables to detect fine vertical structures and consequently middle/upper tropospheric variabilities, it also slightly improves the precision of the HDO/H_2O ratio of the total column.

6 Empirical validation of the innovative approach

We test our novel retrieval method with spectra measured on 116 days between January 2005 and March 2006 at the Izaña Observatory (28°18′ N, 16°29′ W at 2370 m a.s.l., Tenerife, Spain) applying a Bruker IFS 125HR. The IFS 125HR replaced a Bruker IFS 120M, which has already been in operation since February 1999. The measurements form part of the NDACC (Network for Detection of Atmospheric Composition Change; up to 2005 it was called NDSC) activities (Kurylo, 1991, 2000; NDSC, web site). More details about these measurements and the site can be found in Schneider et al. (2005).

The test is done in several steps. First, we compare the H_2O results to ptu-sonde measurements, which gives

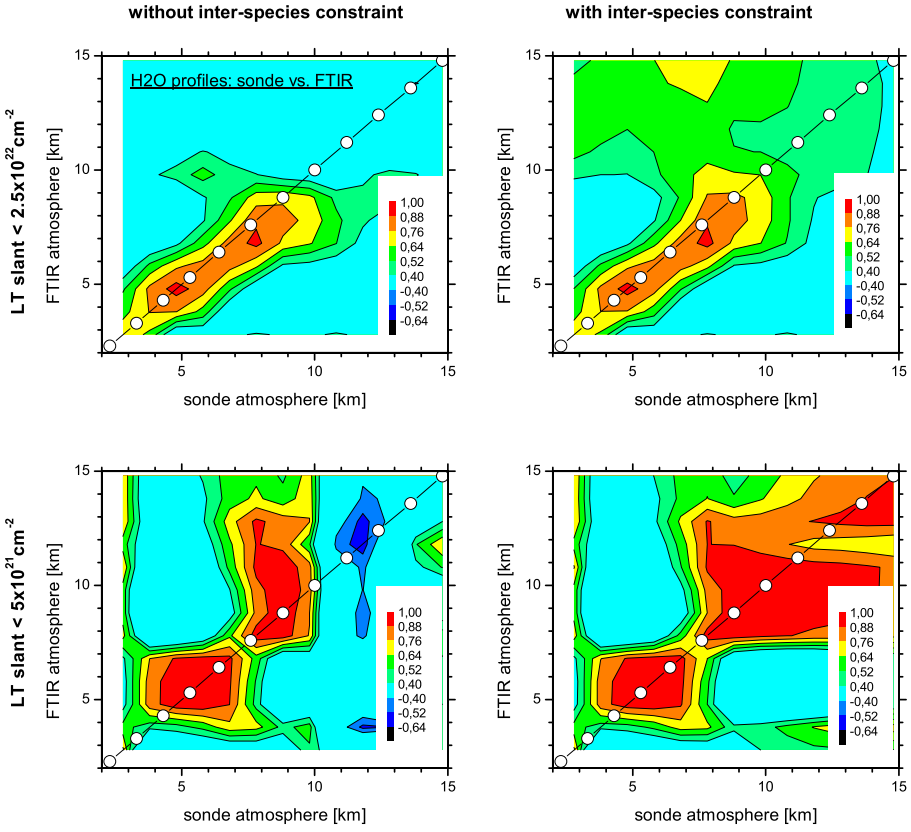

Fig. 19. Correlation matrices between the H_2O measurements of FTIR and ptu-sonde. Left panels: correlations without inter-species constraints; right panels: correlations with inter-species constraints; upper panels: for days with LT slant $<10\times2.5^{22}\mathrm{cm}^{-2}$; lower panels for for days with LT slant $<5\times10^{21}\mathrm{cm}^{-2}$. Colors mark the values of the correlation coefficients (ρ) as given in legend.

valuable information about the quality of the spectroscopic data and the measurements. Second, we look on the statistics of our retrieved δD values. Does it agree with the typical δD profiles obtained from other measurements? Third, we examine if measurements performed on the same day are in agreement with each other. Finally, we show a 15 months record of lower and middle/upper tropospheric δD values and demonstrate by means of isentropic trajectories, that outliers of this record can clearly be identified by unusual transport events.

6.1 Comparison of H_2O profiles to ptu-sonde measurements

Figure 19 validates the FTIR H_2O profiles with ptu-sonde profiles. Shown are matrices of correlations between measured sonde and FTIR profiles. It was required that both measurements are performed within 2 h. The sonde data are corrected by a method suggested by Leiterer et al. (2005). To avoid problems with iced detectors we disregard sondes, which passed layers with a vapour pressure close to the liquid or ice saturation pressure. This exercise was already presented in Schneider et al. (2006) for a period ranging from March 1999 to January 2004 and for FTIR data obtained from the Bruker IFS 120M. Here we investigate the 125 HR spectra and examine if the simultaneous fit of the HDO lines and the inter-species constraint improves the agreement. The left and right panels show the results for the retrieval with and without inter-species constraint, respectively. The upper panels show the situation for LT slant $<2.5\times10^{22}\mathrm{cm}^{-2}$ (comparison of 59 days), the lower panels for LT slant $<5\times10^{21}\mathrm{cm}^{-2}$ (comparison of 7 days). As can be observed the inter-species constraint improves the sensitivity of the FTIR H_2O profile above 8 km. The FTIR profiles are in best agreement with the sonde data for altitudes up to 9 km. Even for moderately saturated lines (LT slant $<2.5\times10^{22}\mathrm{cm}^{-2}$ criterion) the sonde and FTIR amounts correlate with a coefficient of 0.75 at 9 km. In this case upper tropospheric variabilities are only observable in the spectroscopic HDO signatures. Since H_2O is constrained towards HDO, it also benefits from the information only present in the HDO spectra. Furthermore, the FTIR amounts retrieved at this altitude are independent from those below 7 km. Not considering the inter-species constraint only leads to a correlation coefficient of 0.64 at 9 km.

For days with low slant columns between 2.3 and 4.3 km (LT slant $<5\times10^{21}\,\mathrm{cm}^{-2}$), introducing the inter-species

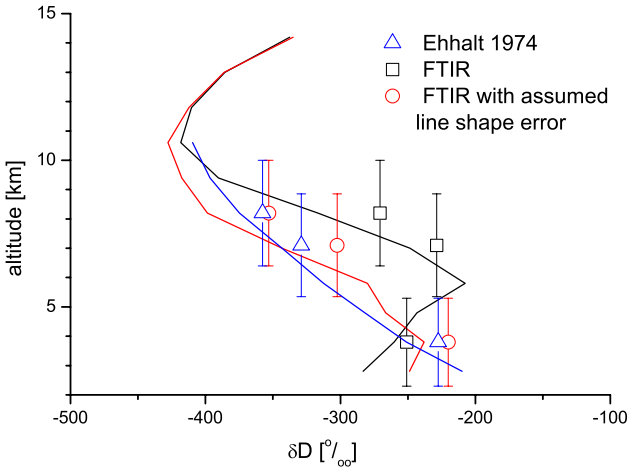

Fig. 20. Comparison of mean δD profiles as obtained by Ehhalt (1974) and our measurements.

constraint provides for good agreement with the sonde up to 12 km. This is a large improvement to the retrievals without inter-species constraint, where the agreement is limited to below 10 km. Unfortunately this comparison only bases on 7 measurement days, which makes their conclusions less robust than those taken from the 59 compared days for the LT slant $<2.5\times10^{22}$cm^{-2} condition.

6.2 Comparison to Ehhalt (1974) measurements

For this validation we calculate the mean of all the δD profiles retrieved between January 2005 and March 2006 and compare them to the mean of the Ehhalt (1974) profiles. The mean of the Ehhalt (1974) profiles is calculated from the simulations of Sect. 5. It is the mean of profiles which take into account the typical vertical resolution of our FTIR retrieval and which obey the statistics of the Ehhalt (1974) measurements. This assures an adequate comparison of the Tenerife δD profiles as measured by the FTIR to the Ehhalt (1974) measurements.

The blue line in Fig. 20 depict the mean of the Ehhalt (1974) profiles. The blue triangles show the mean for the layers as indicated by the error bars. This profile is very similar to the profile of Fig. 1, i.e. the smoothing has no significant impact on the mean of the original fine structured profiles. The black line and squares represent the mean of the Izaña δD profiles as retrieved from the FTIR spectra. It has lower δD values at the lower troposphere and higher δD values at the middle/upper troposphere as compared to the Ehhalt (1974) measurements. Such a δD profile may be caused occasionally by extraordinary transport processes, it presents, however, very unlikely the real mean situation. It is more probable that the observed mean profile is influenced by a systematic error source. Inconsistencies in the pressure broadening coefficients as assumed in Sect. 5.5.2 would produce this kind of systematic error (see mean error as depicted in Fig. 16). If the pressure broadening coefficient (γ) of HDO is overestimated relative to γ of H_2O, the retrieval intends to sharpen the HDO lines by attributing more HDO to the middle/upper troposphere and less to the lower troposphere. The resulting δD would decrease in the lower troposphere and increase in the middle/upper troposphere. The red line and circles in Fig. 20 confirm this systematic error estimation. It shows the mean of the δD profiles retrieved at Izaña applying a by 2 % increased γ of HDO. Under this assumption the mean Izaña profiles are comparable to the mean Ehhalt (1974) profiles. Our measurements suggest that in the HITRAN 2004 database the γ of HDO is by 2% too low as compared to the γ of H_2O. However, this issue needs further examinations, and in the following we still apply the γ values from HITRAN 2004.

6.3 Consistency for measurements performed within 6 h

If the weather conditions permit, we perform two or more FTIR measurements per day. If we assume that there is no significant change of the δD values during one day, this may allow a test of the precision of the measurements. However, a pair of measurements performed within several hours is only partly representative for the highly variable atmospheric conditions encountered by measurements performed on different days or months. Thus, it is no real test of the overall precision. The overall precision is mainly reduced by changing atmospheric conditions, which are responsible for the random component of the smoothing error and the random component of the uncertainties in the pressure broadening coefficients. Changes in the fine structures of the HDO and H_2O profiles will influence the retrieved profiles. And besides, changes in the level of saturation of the absorption lines will affect the averaging kernels and thus the retrieved profiles also in the middle/upper troposphere. The level of saturation depends mainly on the lower tropospheric water vapour amount. We found that both the diurnal variabilities in the fine structures of the HDO and H_2O profiles and in the lower tropospheric water vapour amounts are only half the variabilities occurring over longer timescales. As a consequence this consistency check should underestimate the real overall precision.

Despite these limitations the test allows us to check our assumptions about the parameter and measurement noise errors or if there is an hitherto unknown but important error or if there are problems in the retrieval. Figure 21 shows correlations between δD values measured within 6 h. The left panel depicts the situation for the lower troposphere, the right panel for the middle/upper troposphere. The correlation coefficients of 0.90 and 0.85 lead to a precision for the two measurements together of 44% and 53% (see Eq. 5). Assuming independency of the errors, the precision for one measurement is 31% for the lower troposphere and 37% for the middle/upper troposphere. For the middle/upper troposphere,

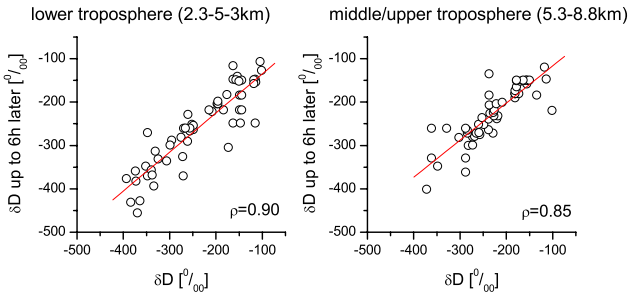

Fig. 21. Correlation between δD obtained within 6 h.

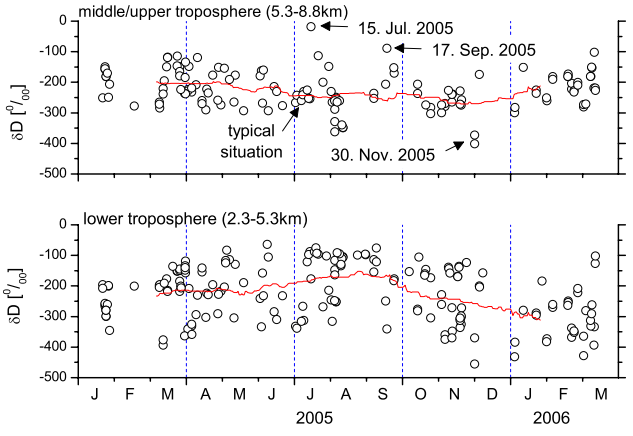

Fig. 22. 15 month record of δD measured above Tenerife. Black circles: individual measurements; red lines: three months running mean; lower panel: lower troposphere; upper panel: middle/upper troposphere when LT slant $<2.5\times10^{22}$cm^{-2}.

this is in good agreement with the estimated overall precision of 50% (Table 2). For the lower troposphere, the value is too large as compared to the estimated 15%. A reason may be that in the boundary layer the assumption of a constant δD over 6 h is not valid. In this case the calculated 31% would be the sum of the precision of the retrieval and the 6 h-variability of δD for the lower troposphere.

6.4 15 months δD record and its interpretation by isentropic trajectories

Figure 22 shows the middle/upper and lower tropospheric δD values obtained from the FTIR measurements. Concerning the lower tropospheric amounts we observe an annual cycle with largest values in late summer and lowest values in late winter. This cycle is associated to the sea and air temperature: The higher the sea and air temperatures the lower the isotope fractionation during evaporation.

The variabilities in the upper/middle troposphere are mainly correlated to transport processes. We demonstrate this by means of the outliers seen in the upper panel of Fig. 22. On 15 July and 17 September 2005 extraordinary

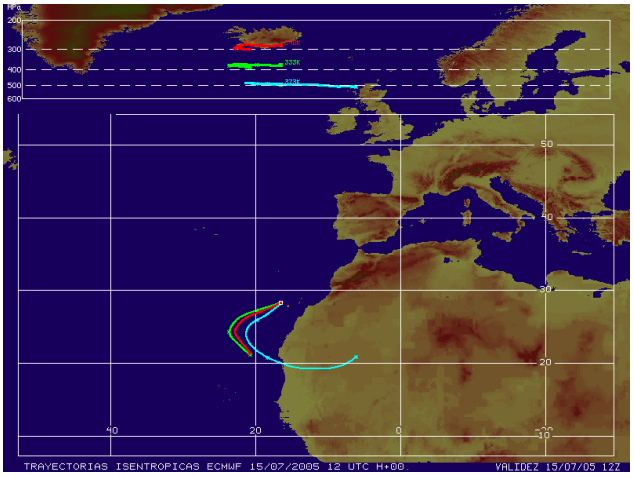

Fig. 23. Isentropic trajectories for the last 60 h and for airmasses arriving above Tenerife on 15 July 2005 at 6 (cyan), 8 (green), and 10 km (red). Upper part shows projection on longitude – pressure plane: the pressure griding marks 600, 500, 400, 300, and 200 hPa levels. Lower part shows longitude–latitude plane: the longitude griding is in steps of 20° and the latitude griding in steps of 10°.

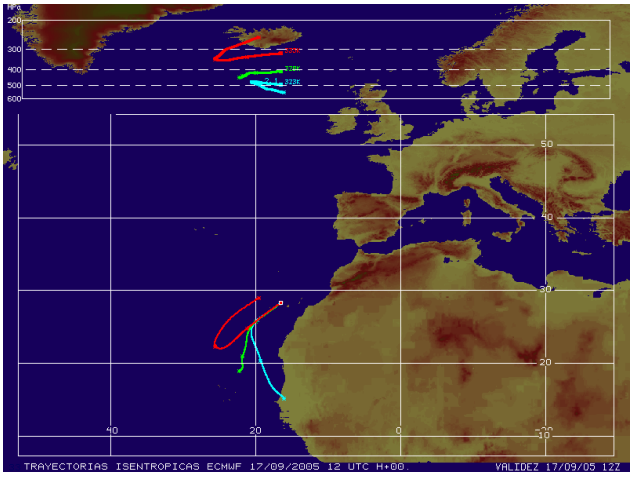

Fig. 24. Same as Fig. 23 but on 17 September 2005.

high δD values are observed. The 60 h isentropic trajectories for these days are shown in Figs. 23 and 24. The trajectories reveal that on both days we detected tropical airmasses, which very likely experienced strong tropical convection. Strong tropical convection results in strongly increased δD values. To the contrary, on 30th of November 2005 we detect very low δD values. Looking on the isentropic trajectories explains this observation (Fig. 25): the relevant airmass originates from relatively high latitudes, and it descended strongly during the last 12 h before arriving above Tenerife. It comes from a region where δD values are much lower than the typical δD at the middle/upper troposphere over Tenerife. This unusual strong descent is associated to

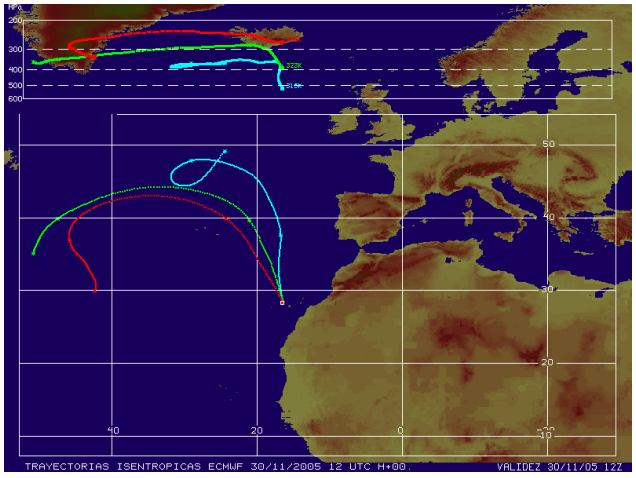

Fig. 25. Same as Fig. 24 but on 30 November 2005.

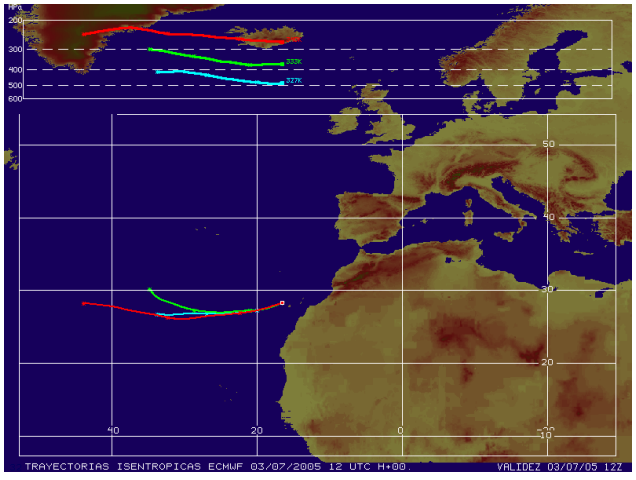

Fig. 26. Same as Fig. 24 but on 3 July 2005.

the pass of ex-tropical storm Delta just 36 h prior to the measurement. During summer Izaña is situated close to the Inner Tropical Convergence Zone (ITCZ). Then occasionally airmasses originating from the ITCZ are present above Izaña, leading to very high delta δD. However, even during summer low δD values are possible. For example, on 4 and 11 August when we detected airmasses from higher latitudes, i.e. airmasses originating from a statically more stable atmosphere. In the absence of wave perturbations middle/upper tropospheric winds are westerlies. The detected airmasses origin is the central subtropical Atlantic. Figure 26 shows such typical trajectories.

The outliers are statistically significant: The whole ensemble of middle/upper tropospheric δD values has a mean and standard deviation of –223+/-61 per mil, while for a high latitude airmass it is typically below –350 per mil and for a tropical airmass above –100 per mil. This demonstrates that the achievable precision is sufficient to distinguish between different origins and thus different vertical transport processes or atmospheric conditions experienced by the detected water vapour amounts.

Our observations underline the importance of transport processes for the middle/upper tropospheric δD value: for a pure Rayleigh distillation the δD values should be generally higher in summer, due to a warmer atmosphere, than in winter. Our measurements reveal no such annual cycle. In contrary, they even indicate that middle/upper tropospheric δD values are highest in spring and lowest in autumn. The δD observations are a good marker for middle/upper tropospheric transport processes or for the statical stability at the origin of the detected airmasses.

7 Summary and conclusions

We propose an innovative approach for retrieving profiles of trace gas ratios. While common methods are only optimal estimators for both retrieved trace gases our approach considers the a-priori knowledge of the ratio profiles and is thus an optimal estimation method for the ratio profiles. For ground-based FTIR measurements, we estimated the precision achievable with this approach for HDO/H_2O profiles and compared it to the precision of the common approach. We found that only by our method a precision necessary to detect variabilities of the middle/upper tropospheric HDO/H_2O ratios can be achieved. The measurements need not to be performed from mountain observatories. Free tropospheric HDO/H_2O ratios can also be detected when the applied H_2O lines are moderately saturated (see example of Fig. 3).

Beside the smoothing error the most important errors in the retrieved δD values are due to uncertainties in the spectroscopic line parameters. A higher accuracy of the HDO and H_2O line shape parameters in the 1000–1330 cm^{-1} region would further improve the precision of the retrieved ratios. We found that errors due to uncertainties in the alignment of the sun-tracker, the temperature profile or the instrumental line shape are of secondary importance. This alleviates the retrieval of precise and consistent δD values even under changing or poorly documented instrumental performance – a great advantage when aiming on consistent long-term records of δD values by applying historic FTIR measurements.

An important potential application of our proposed approach is the analysis of annual cycles at different measurement sites. Annual cycles of δD values, which have a large day-to-day variability, can only be determined by continuous measurements. Ground-based FTIR measurements are performed continuously. This is the decisive advantage of our proposed method over more precise but sparsely performed balloon- or aircraft-based in-situ measurements. In future work the annual cycles retrieved for various measurement sites could help to constrain models (e.g. Schmidt et

al., 2005) and contribute to a better understanding of vertical water vapour transport, which is an important uncertainty in climate simulations.

The proposed method can be applied for the retrieval of other isotope ratio profiles (e.g. CO_2, CH_4, O_3,...). Furthermore, it can be applied for the retrieval of strongly correlated trace gases, like e.g. CH_4 and N_2O. In this case the method should improve the precision and accuracy of both trace gas profiles. The results of this study strongly recommend the application of our approach whenever strongly correlated trace gases are the objective. It could be adapted to a wide range of retrieval codes, including satellite codes, for the inversion of limb sounder as well as nadir spectra.

Acknowledgements. We would like to thank the European Commission for funding via the projects UFTIR (contract EVK2-CT-2002-00159-UFTIR) and SCOUT-O3 (contract GOCE-CT-2004-505390-SCOUT-O3). Furthermore, we are grateful to J. J. Bustos for performing the trajectory calculations and to the Goddard Space Flight Center for providing the temperature and pressure profiles of the National Centers for Environmental Prediction via the automailer system.

Edited by: T. Röckmann

References

Abbas, M. M., Guo, J., Carli, B., Mencaraglia, F., Bonetti, A., Carlotti, M., and Nolt, I. G.: Stratospheric O_3, H_2O, and HDO distributions from balloon-based far-infrared observations, J. Geophys. Res., 92, 8354–8364, 1987.

Ehhalt, D. H.: Vertical profiles of HTO, HDO, and H_2O in the Troposphere, Rep. NCAR-TN/STR-100, Natl. Cent. for Atmos. Res., Boulder, Colo., 1974.

Gedzelman, S. D.: Deuterium in water vapor above the atmospheric boundery layer, Tellus, 40B, 134–147, 1988.

Hase, F., Blumenstock, T., and Paton-Walsh, C.: Analysis of the instrumental line shape of high-resolution Fourier transform IR spectrometers with gas cell measurements and new retrieval software, Appl. Opt., 38, 3417–3422, 1999.

Hase, F., Hannigan, J. W., Coffey, M. T., Goldman, A., Höpfner, M., Jones, N. B., Rinsland, C. P., and Wood, S. W.: Intercomparison of retrieval codes used for the analysis of high-resolution, ground-based FTIR measurements, J. Quant. Spectrosc. Radiat. Transfer, 87, 25–52, 2004.

Höpfner, M., Stiller, G. P., Kuntz, M., Clarmann, T. v., Echle, G., Funke, B., Glatthor, N., Hase, F., Kemnitzer, H., and Zorn, S.: The Karlsruhe optimized and precise radiative transfer algorithm, Part II: Interface to retrieval applications, SPIE Proceedings 1998, 3501, 186–195, 1998.

Kuang, Z., Toon, G. C., Wennberg, P. O., and Yung, Y. L.: Measured HDO/H_2O ratios across the tropical tropopause, Geophys. Res. Lett., 30(7), 1372, doi:10.1029/2003GL017023, 2003.

Kuntz, M., Höpfner, M., Stiller, G. P., Clarmann, T. v., Echle, G., Funke, B., Glatthor, N., Hase, F., Kemnitzer, H., and Zorn, S.: The Karlsruhe optimized and precise radiative transfer algorithm, Part III: ADDLIN and TRANSF algorithms for modeling spectral transmittance and radiance, SPIE Proceedings 1998, 3501, 247–256, 1998.

Kurylo, M. J.: Network for the detection of stratospheric change (NDSC), Proc. SPIE–Int. Co. Opt. Eng. 1991, 1491, 168–174, 1991.

Kurylo, M. J. and Zander, R.: The NDSC – Its status after 10 years of operation, Proceedings of XIX Quadrennial Ozone Symposium, Hokkaido University, Sapporo, Japan, 167–168, 2000.

Leiterer, U., Dier, H., Nagel, D., Naebert, T., Althausen, D., Franke, K., Kats, A., and Wagner, F.: Correction Method for RS80-A Humicap Humidity Profiles and their Validation by Lidar Backscattering Profiles in Tropical Cirrus Clauds, J. Atmos. Oceanic Technol., 22, 18–29, 2005.

Meier, A., Toon, G. C., Rinsland, C. P., Goldman, A., and Hase, F.: Spectroscopic Atlas of Atmospheric Microwindows in the Middle Infrared, 2nd Edition, IRF Technical Report 048, ISSN 0284-1738, Kiruna, Sweden, 2004.

NDSC: http://www.ndsc.ws/, 2005.

Rodgers, C. D.: Inverse Methods for Atmospheric Sounding: Theory and Praxis, World Scientific Publishing Co., Singapore, 2000.

Rodgers, C. D. and Connor, B. J.: Intercomparison of remote sounding instruments, J. Geophys. Res., 108(D3), 4116–4128, 2003.

Rothman, L. S., Barbe, A., Benner, D. C., Brown, L. R., Camy-Peyret, C., Carleer, M. R., Chance, K. V., Clerbaux, C., Dana, V., Devi, V. M., Fayt, A., Fischer, J., Flaud, J.-M., Gamache, R. R., Goldman, A., Jacquemart, D., Jucks, K. W., Lafferty, W. J., Mandin, J.-Y., Massie, S. T., Newnham, D. A., Perrin, A., Rinsland, C. P., Schroeder, J., Smith, K. M., Smith, M. A. H., Tang, K., Toth, R. A., Vander Auwera, J., Varanasi, P., and Yoshino, K.: The HITRAN Molecular Spectroscopic Database: Edition of 2000 Including Updates through 2001, J. Quant. Spectrosc. Radiat. Transfer, 82, 5–44, 2003.

Rothman, L. S., Jacquemart, D., Barbe, A., Benner, D. C., Birk, M., Brown, L. R., Carleer, M. R., Chackerian Jr., C., Chance, K. V., Coudert, L. H., Dana, V., Devi, J., Flaud, J.-M., Gamache, R. R., Goldman, A., Hartmann, J.-M., Jucks, K. W., Maki, A. G., Mandin, J.-Y., Massie, S. T., Orphal, J., Perrin, A., Rinsland, C. P., Smith, M. A. H., Tennyson, J., Tolchenov, R. N., Toth, R. A., Vander Auwera, J., Varanasi, P., and Wagner, G.: The HITRAN 2004 molecular spectroscopic database, J. Quant. Spectrosc. Radiat. Transfer, 96, 139–204, 2005.

Schmidt, G. A., Hoffmann, G., Shindell, D. T., and Hu, Y.: Modeling atmospheric stable water isotopes and the potential for constraining cloud processes and stratosphere-troposphere water exchange, J. Geophys. Res., 110, D21314, doi:10.1029/2005JD005790, 2005.

Schneider, M., Blumenstock, T., Chipperfield, M., Hase, F., Kouker, W., Reddmann, T., Ruhnke, R., Cuevas, E., and Fischer, H.: Subtropical trace gas profiles determined by ground-based FTIR spectroscopy at Izaña (28° N, 16° W): Five year record, error analysis, and comparison with 3-D-CTMs, Atmos. Chem. Phys., 5, 153–167, 2005, http://www.atmos-chem-phys.net/5/153/2005/.

Schneider, M., Hase, F., and Blumenstock, T.: Water vapour profiles by ground-based FTIR spectroscopy: study for an optimised retrieval and its validation, Atmos. Chem. Phys., 6, 811–830, 2006, http://www.atmos-chem-phys.net/6/811/2006/.

Stiller, G. P., Höpfner, M., Kuntz, M., Clarmann, T. v., Echle, G.,

Fischer, H., Funke, B., Glatthor, N., Hase, F., Kemnitzer, H., and Zorn, S.: The Karlsruhe optimized and precise radiative transfer algorithm, Part I: Requirements, justification and model error estimation, SPIE Proceedings 1998, 3501, 257–268, 1998.

Taylor, C. B.: The vertical variations of the isotopic concentrations of tropospheric water vapour over continental Europe and their relationship to tropospheric structure, N. Z. Dep. Sci. Ind. Res., Inst. Nucl. Sci. Rep. INS-R-107, 44 pp., 1972.

Wilks, D. S.: Statistical methods in the atmospheric science, Academic Press, ISBN 0-12-751965-3, 1995.

Zahn, A.: Constraints on 2-Way Transport across the Arctic Tropopause Based on O_3, Stratospheric Tracer (SF_6) Ages, and Water Vapor Isotope (D, T) Tracers, J. Atmos. Chem. 39, 303–325, 2001.